Construction and Building Materials 107 (2016) 272–286

Contents lists available at ScienceDirect

Construction and Building Materials

journal homepage: www.elsevier.com/locate/conbuildmat

Waste-glass fume synthesized using plasma spheroidization technology: Reactivity in cement pastes and mortars

D. Harbec [a,*], A. Tagnit-Hamou [a], F. Gitzhofer [b]

[a] CRIB, Department of Civil Engineering, Université de Sherbrooke, 2500, boul. de l'Université, Sherbrooke, Quebec J1K 2R1, Canada
[b] CREPE, Department of Chemical Engineering, Université de Sherbrooke, 2500, boul. de l'Université, Sherbrooke, Quebec, Canada

HIGHLIGHTS

- Synthesis of glass fume (GF) as alternative to silica fume (SF) from waste glass.
- GF has a complete spherical morphology with diameter of 30–200 nm.
- Comparatively to SF, GF improve the rheological properties of cement mortars.
- In a short term, the alkali of GF dissolves and activates the hydration of cement.
- On a long term, the amorphous silica of GF reacts pozzolanically with portlandite.
- GF Mortars achieves comparable compressive strength than that of SF mortars.

GRAPHICAL ABSTRACT

FEGSEM micrograph of GF nanoparticles.

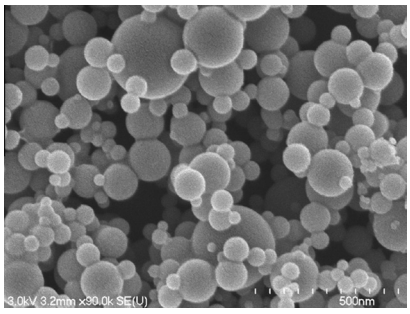

ARTICLE INFO

Article history:
Received 5 October 2015
Received in revised form 4 January 2016
Accepted 7 January 2016
Available online 20 January 2016

Keywords:
Glass fume
Spheroidized nanoparticles
Nanosilica
Plasma spheroidization
Cement hydration
Glass fume hydration

ABSTRACT

Using silica-based nanoparticles is one way to stimulate the hydration reactivity and improve the rheological properties of concrete, given their fineness and spherical shape. Based on its high content in amorphous silica ($(SiO_2 > 70$ wt.%), waste glass is an excellent material for valorization into pozzolanic nanoparticles or the so-called "glass fume" (GF). GF, produced using the radiofrequency induction-coupled-plasma (RF ICP) spheroidization technology, mainly consists of spherical and amorphous nanoparticles (dia. of 30–200 nm). Given the scarcity and high cost silica fume (SF), its use in producing high-strength concrete is now limited. GF produced using the scalable plasma spheroidization process is currently being tested in cement-based products as an alternative for SF.

The GF was characterized with field-emission-gun scanning electron microscopy (FEGSEM), transmission electron microscopy (TEM), Brunauer–Emmett–Teller (BET) specific surface, acoustic particle sizer (APS), X-ray fluorescence (XRF) and thermogravimetry coupled to mass spectrometry (TGA-MS). The hydration of GF in cement pastes and mortars was monitored in this study. The cement pastes were

Abbreviations: σ_E, electrical conductivity; AFM, calcium monosulfoaluminate crystals; Aft, ettringite; APS, acoustic particle sizer; BET, Brunauer–Emmett–Teller method; CH, portlandite; C–S–H, hydrated calcium silicate; DTA, differential temperature analyses; DTG, derivative thermogravimetric curve; EDS, energy-dispersive spectroscopy; FEGSEM, field-emission-gun scanning electron microscopy; GF, glass fume; GP, waste-glass powder; GU cement, general-use portland cement; HDPE, high-density polyethylene; ITZ, interfacial transition zone; LOI, Loss on ignition; PCA, polycarboxylate; PNS, polynaphthalene-sulfonate; PSD, particle-size distribution; PSR, particle-size range; RF ICP, radiofrequency induction-coupled-plasma; SCM, supplementary cementitious material; SF, silica fume; SP, superplasticizer; SSA, specific surface area; TEM, transmission electron microscopy; TGA, thermogravimetric analysis; TGA-MS, thermogravimetry analysis coupled to mass spectrometry; VPSEM, variable pressure scanning electron microscopy; W/B, water-to-binder ratio; XRD, X-ray diffraction; XRF, X-ray fluorescence.

* Corresponding author.
E-mail addresses: David.harbec@usherbrooke.ca (D. Harbec), arezki.tagnit-hamou@usherbrooke.ca (A. Tagnit-Hamou), Francois.gitzhofer@usherbrooke.ca (F. Gitzhofer).

http://dx.doi.org/10.1016/j.conbuildmat.2016.01.011

Nucleation sites
Alcali activation
Pozzolanic reaction
Cementitious matrix
Densification

characterized at early age with isothermal calorimetry and as a function of curing time with X-ray diffraction (XRD) as well as with thermogravimetric analysis (TGA) and variable pressure scanning electron microscopy (VPSEM). Mortars were tested for compressive strength and their microstructure was observed with VPSEM. Also, their hydration was monitored with the electrical conductivity. The results indicate that GF offers nucleation sites for portlandite, alkalis for the activation of the cement hydration at early age, and a pozzolanic behavior for the long-term evolution of mortar properties. In mortars, the GF yielded compressive strengths equivalent to those obtained with SF used as a comparison. The GF mortars required a lower superplasticizer (SP) dosage than the SF mortar because of the ball-bearing effect induced by GF's complete spherical morphology. In addition to spherical nanoparticles, SF contains silica-based nanofilaments, which affect the rheology of fresh cement-based materials.

1. Introduction

Because of its high pozzolanic reactivity and filler effect, submicron amorphous silica has been added especially to high-performance [1] and reactive-powder [2,3] concretes over the past 30 years. Silica fume (SF) is a supplementary cementitious material (SCM) used as cement replacement that improves mechanical performance [4,5], decreases porosity, and densifies microstructure [6–11]. Today, with the emergence of nanotechnologies, new cement and concrete materials with improved properties can be developed by using nanomaterials such as nanosilica [12–23]. Due to its high specific surface and amorphous silica content, nanosilica possesses nucleation sites for cement hydrates. It can be used as a highly reactive SCM and it improves the compacity of cement-based materials. The benefits of nanosilica include the promotion of cement hydration, pozzolanic reaction, and densification of the cement-paste microstructure [12,16,17,19–21]. Many researchers reported that nanosilica reduces the workability [15–17] and shortens the setting time of cement-based materials [17,19–21]. The influence of nanosilica on the polymerization of hydrated calcium silicate (C–S–H) gels has also been monitored using ^{29}Si MAS NMR analyses [22,23]. Dolado et al. [22] and Kontoleontos et al. [19] observed that the addition of nanosilica increased the mean chain length of C–S–H, and Brykov et al. [23] demonstrated a 7–10% increase in the polymeric silicon–oxygen fraction.

Nanoparticles can be manufactured using two main approaches: (i) the top-down approach, in which larger structures are reduced in size to the nanoscale, and (ii) the bottom-up approach, in which materials are engineered from atoms or molecular components through a process of assembly or self-assembly resulting in nanoparticles [12]. Based on its high content in amorphous silica (SiO_2 > 70 wt.%), waste glass can be transformed into amorphous silica-based nanoparticles using a top-down manufacturing process.

Today, the cost of SF continues to climb due to limited availability. As a result, GF is being synthesized at the laboratory-scale using the radiofrequency induction-coupled-plasma (RF ICP) spheroidization of waste-glass powder (GP) [24] as a potential alternative to SF. At the laboratory-scale the RF ICP spheroidization technology consumes between 130 and 240 kWh/kg of GP, which is in the same order of magnitude than the thermal transferred arc technology [25] normally used to produce industrial grade SF [5,26]. This paper begins by providing a complete material characterization of GF, followed by the results of tests and measurements made on cement pastes and mortars.

2. Materials and methodology

GF was synthesized at the laboratory-scale using RF ICP spheroidization technology. GP with a particle-size distribution of 1–100 μm was fed into 50 kW RF ICP torch. The high-temperature plasma flame (≈8000 K) initially vaporized the GP, reducing it to nanoclusters. Depending on the temperature gradients in the plasma flame, the nanoclusters coalesced and coagulated, self-assembling into glass nanodroplets. Downstream, these nanodroplets traveled through a colder temperature region where the GF was formed. The GF was collected on both the reactor and filter walls as previously described by Harbec et al. [24].

In this investigation, SF is used as a comparison material for GF. Similarly to GF, SF is produced with a plasma process. It is a by-product of the silicon metal manufacturing process, based on a plasma arc reduction of quartz. In this process, silicon monoxide vapors ($SiO_{(g)}$) escape from the plasma arc furnace and oxidize when entering in contact with air into amorphous SiO_2 particles [5,26].

2.1. Material characterization

The size and morphology of the GF and SF were observed under different types of electron microscopy. Given their nanometric size, the GF and SF were observed using field emission gun scanning electron microscopy (FEGSEM) and transmission electron microscopy (TEM). The FEGSEM acceleration voltage and emission current were, respectively, 3.0 kV and 10 μA. The TEM acceleration voltage was 80 kV. Prior to the electron microscopy observations, 0.2 g of GF and SF was dispersed in ethanol using an ultrasonic probe. For the FEGSEM observations, a drop of the resulting suspension was deposited on a silicon wafer and metallized with platinum (Pt) to ensure the sample's surface conductivity. For the TEM observations, a drop of the suspension was deposited on a copper grid coated with a carbon film.

Specific surface area (SSA), nanocontent, chemical composition, and crystallinity of the GF were also compared to those of SF. The SSA was measured with the Brunauer, Emmett, and Teller (BET) method. The measurements were performed on 5 adsorption isotherms using nitrogen (N_2).

The particle-size distribution (PSD) of the GF was measured in distilled water with an acoustic particle sizer (APS) coupled with zeta potential to measure the stability of the suspension. The dispersion quality of any type of nanomaterial (nanoparticles, nanofibers) in a cementitious matrix remains an important issue for mortar and concrete performance [12,14,27]. To investigate the dispersion of the nanoparticles, PSD measurements were performed on GF slurries mixed with a spatula and on an ultrasonic-dispersed GF slurry. The nanocontent of the GF and SF were determined via settling of the microparticles in ethanol dispersion, as described in [24]. Chemical composition and crystallinity were determined, respectively, with X-ray fluorescence (XRF) and X-ray diffraction (XRD) techniques in the 10–70° 2θ range. Loss on ignition (LOI) was measured with thermogravimetry analysis coupled to mass spectrometry (TGA-MS).

2.2. Tests on cement pastes

Tests were performed on cement pastes to investigate the influence of the GF on pozzolanic reactivity and heat of hydration when in contact with calcium hydroxide and cement. First, the pozzolanic reaction was characterized when the GF was mixed solely with portlandite ($Ca(OH)_2$: CH). Second, the pozzolanic reaction and heat of hydration were characterized in cement pastes, in which the GF served as partial replacement of general-use portland cement (GU cement).

First, the GF and silica fume (SF) were mixed separately with an analytical grade crystalline CH to investigate and compare their pozzolanic reactivity. A fixed amount of 5 g of dry powder (GF + CH and SF + CH) was blended in different proportions in sealed polymer bottles. Dry-powder mixes of GF + CH and SF + CH (Table 1) were analyzed with XRD prior to the addition of water in order to calibrate the CH XRD peak intensity (2θ = 34.09°) versus the initial CH content in the mix. These analyses are used to build a calibration curve for GF + CH and SF + CH mixes. The 14 test specimens were then mixed with deionized water at a water-to-binder ratio (W/B) of 1 (Table 1) in a glove box under argon atmosphere at 25 °C. After 1, 7, and 28 days of hydration, the pastes were immersed in isopropanol for 24 h to stop the hydration. The pastes were then removed from the isopropanol and placed in a fume hood for drying. After drying, the samples were ground with an agate mortar and tested with XRD for free unreacted CH content quantified with the calibration curve as described by Alhozaimy et al. [28]. This method is suitable for the type of mixtures analyzed (GF + CH and SF + CH) since it assumes that CH remains crys-

talline during hydration. The microstructures of the pastes were also observed with a variable-pressure scanning electron microscope (VPSEM) coupled with energy-dispersive spectroscopy (EDS).

The hydration and pozzolanic reactions were also evaluated by mixing GF with GU cement. Table 2 presents three cement-paste batches with a W/B of 0.4. For each batch, 150 g of binder (GU cement + GF) was mixed with 60 g of water for 2 min with an electric hand mixer. The GF was introduced into the paste batches as 0% (T0), 5% ($T5_{GF}$), and 10% ($T10_{GF}$) replacements of GU cement for long-term reactivity tests.

The batches were cast in sealed 15 mL plastic tubes for hardening. Reactivity tests were performed using thermogravimetry (TGA) and differential temperature analyses (DTA) combined to the derivative thermogravimetric curve (DTG) after 1, 3, 7, 14, 28, and 56 days of hydration to quantify the combined water and CH. TGA is rather recommended for this part of the study, because the CH generated from the portland cement hydration can be of different crystalline and amorphous structures [28]. At the end of each hydration time period, the hardened cement pastes were crushed and immersed in isopropanol for 24 h in order to stop the hydration. The samples were then placed in a fume hood for drying. After drying, the samples were ground with an agate mortar and tested for combined water and portlandite content.

Isothermal calorimetry was used to monitor the heat of hydration of the cement pastes incorporating 1% ($C1_{GF}$), 5% ($C5_{GF}$) and 10% ($C10_{GF}$) GF during the first 24 h of hydration (Table 3). The heats of hydration of these cement pastes containing GF were compared to those of a control cement paste (C0) and a paste containing 10% SF ($C10_{SF}$) as a cement replacement. The cement pastes were mixed separately with GU cement at W/B = 0.4.

Isothermal calorimetry tests were conducted according to ASTM C1702 method B. The cement pastes containing 3.0 g of binder (Table 3) were tightly sealed inside a 20 mL high-density polyethylene (HDPE) ampoule immediately after mixing for 2 min and then placed inside an isothermal calorimeter. Ten minutes were required to equilibrate the calorimeter at the measurement temperature of 23 °C. The samples were placed inside the calorimeter about 2 min after the initial contact of the solids and water. Ten additional minutes were required to equilibrate the calorimeter. Thus, the very exothermic, early rapid dissolution of the cement phases was not completely acquired. The total heat of hydration was then computed from the 12th minute of hydration for 24 h.

2.3. Tests on mortars

The mortar batches were blended according to ASTM C305 using GU cement and Ottawa sand, a reference quartz sand used in North America [ASTM C778]. Mortar cubes measuring 50 mm × 50 mm × 50 mm were cast and tested for compressive strength according to ASTM C109/C109M.

Table 4 presents the mix designs for the mortars. The mixes were made with 740 g of binder and a sand-to-binder ratio of 2.75. The mortars were blended at a W/B = 0.484 (indexed A) and at a W/B = 0.40 (indexed B). The GF was incorporated in the mortar batch as 1% ($M1GF_{A,B}$) 5% ($M5GF_{A,B}$), and 10% ($M10GF_{A,B}$) cement replacements. Prior to adding the GU cement in the mixer, the GF was dispersed with an ultrasonic probe for 30 min, resulting in a stable milky-white slurry. The GU cement and sand were then successively added to the GF slurry. At a W/B = 0.484, the various mortar batches had their flows adjusted with a polynaphthalene-sulfonate (PNS) superplasticizer (SP) to achieve 120–170% flow. For W/B = 0.40, the mortar batch flow was adjusted with a polycarboxylate (PCA) SP to achieve 130–200% flow. The mortar flow was measured according to ASTM C1437. Such a high percentage of flow was selected to ensure a good workability of GF and SF fresh mortars Table 4 indicates that the SP dosage generally increases with the GF and SF dosages. Although Garcia-Taengua et al. [17] evidenced that the compressive strength increase with SP dosage, mortars incorporating the same content in GF and SF were dosed with a comparable quantity of SP.

Table 1
Mix based on 5 g of powder to determine pozzolanic reactivity with XRD; W/B = 1.

Mix label X (for XRD)	CH (g)	CH (%)	SF (%)	GF (%)
$X0_{SF}$	0	0	100	0
$X0_{GF}$	0	0	0	100
$X5_{SF}$	0.25	5	95	N/A
$X5_{GF}$	0.25	5	N/A	95
$X9_{SF}$	0.50	9	91	N/A
$X9_{GF}$	0.50	9	N/A	91
$X13_{SF}$	0.75	13	87	N/A
$X13_{GF}$	0.75	13	N/A	87
$X17_{SF}$	1.00	17	83	N/A
$X17_{GF}$	1.00	17	N/A	83
$X20_{SF}$	1.25	20	80	N/A
$X20_{GF}$	1.25	20	N/A	80
$X23_{SF}$	1.50	23	77	N/A
$X23_{GF}$	1.50	23	N/A	77

Table 2
Mixes based on 150 g of binder (GU cement + GF) and W/B = 0.4 to measure reactivity using TGA-DTA.

Mix label T (for TGA)	GF (g)	GF (%)
T0	0	0
$T5_{GF}$	7.5	5
$T10_{GF}$	15	10

Table 3
Mixes based on 3 g of binder and a W/B = 0.4 to measure the heat of hydration using isothermal calorimetry.

Mix label C (for calorimetry)	GF (g)	GF (%)	SF (g)	SF (%)
C0	0	0	0	0
$C1_{GF}$	0.03	1	0	0
$C5_{GF}$	0.15	5	0	0
$C10_{GF}$	0.3	10	0	0
$C10_{SF}$	0	0	0.3	10

For W/B = 0.484, the compressive strengths of hardened mortar cubes containing GF were compared to those of the control mortars ($M0_A$) and mortar containing 10% of SF ($M10SF_A$) as cement replacement. This replacement rate was set according to the accelerated pozzolanic-strength-activity index-test protocol described in ASTM C1240 for the use of silica fume. For W/B = 0.40, the compressive strength of the GF mortar cubes are compared to those of a control ($M0_B$) mortar and mortars containing 1% ($M1SF_B$) and 5% ($M5SF_B$) SF. The hydration kinetics of these mortars, except $M1SF_B$, were monitored via electrical conductivity measurements of the pore solution as described by Bonneau et al. [29].

3. Material characterization

3.1. Electron-microscopy characterization

As can be seen in the FEGSEM and TEM micrographs in Figs. 1 and 2, the GF particles had a spherical morphology with a bimodal size range comprising 97–98 wt.% of nanoparticles (dia. of 30–200 nm) and 2–3 wt.% in microparticles (dia. of 1–10 μm). As shown in Fig. 2, the fineness of the GF particles resulted in a certain degree of agglomeration.

Fig. 3 provides TEM micrographs of the SF, which had a particle size similar to that of the GF, although it did contain some silica-based nanofilaments 15–30 nm in diameter and 200 nm–1 μm in length. This SF is of industrial grade. These filaments may result from the presence of SF particles in a temperature window with sufficient residence time to be plasma-activated for their elongation [30].

Table 4
Mix design of the mortar based on 740 g of binder and S/B = 2.75 (2035 g of Ottawa sand).

Mix label M (for mortar)	GU Cement (g)	Water (g)	SP (% dry extract)	GF (g)	GF (%)	SF (g)	SF (%)	% Flow (ASTM C1437)
$M0_A$	740	355.4	0.27*					150
$M1GF_A$	732.6	355.7	0.24*	7.4	1			170
$M5GF_A$	703	355.9	0.22*	37	5			150
$M10GF_A$	666	353.3	0.66*	74	10			170
$M10SF_A$	666	350.9	0.71*			74	10	120
$M0_B$	740	290.6	0.33#					171
$M1GF_B$	732.6	288.7	0.39#	7.4	1			140
$M5GF_B$	703	288.5	0.46#	37	5			140
$M10GF_B$	666	287.7	0.92#	74	10			130
$M1SF_B$	732.6	288.4	0.46#			7.4	1	200
$M5SF_B$	703	288.1	0.48#			37	5	140

* SP is PNS based.
\# SP is PCA based.

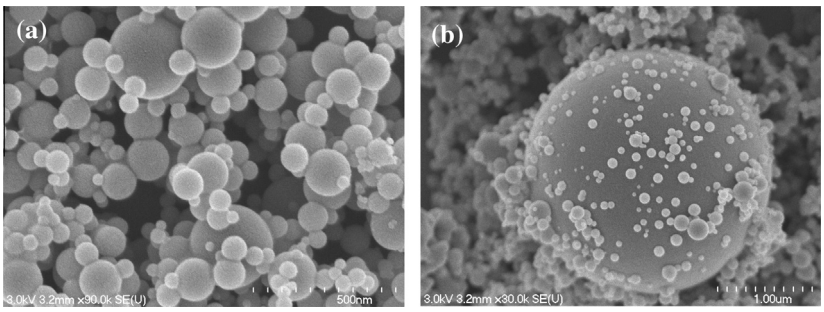

Fig. 1. (a) FEGSEM micrograph of GF nanoparticles. (b) FEGSEM micrograph of GF microparticles.

3.2. SSA and PSD

Table 5 presents the SSA, the particle-size range (PSR), and the nanometric wt.% content of the GF and SF. These were measured, respectively, with BET, electron microscopy (FEGSEM and TEM), and the settling of the microparticles in ethanol. The GF had a lower SSA than the SF, but a similar nanometric PSR and wt.% content. The higher SSA of the SF is related to its different nanofeatures (Fig. 3). The SF incorporates silica-based nanofilaments that increase SSA. However, the SSA and the nanometric content of GF are clearly improved with respect to the results obtained previously [24]. Optimization work has been conducted on the plasma spheroidization process, especially on the process of feeding GP into the RF ICP torch. GP is now preliminarily heated to 80 °C and sieved with 600 μm mesh to remove residual humidity and agglomerations. GP can now be fed at 6.75 g/min with an appreciable fluidity for an efficient vaporization in the plasma torch. This feed rate is, moreover, higher than those tested previously [24].

Fig. 4 provides the resulting PSD curves of the nanometric fraction for each slurry: undispersed (GF) and ultrasonically dispersed (sonicated GF). This figure shows a shift towards a finer PSD when the GF was dispersed. The undispersed slurry evidenced a large lumps distribution hump lying between 0.01 μm and 0.60 μm with a zeta-potential of 5.74 mV. After sonication, the PSD curve became trimodal with a significant dispersion of the nanoparticles and an increase of the absolute value of zeta potential (−12.7 mV). The initial hump breaks down into three granulometry families: the first lying between 0.01 μm and 0.25 μm, the second between 0.25 μm and 0.38 μm, and the third between 0.38 μm and 0.52 μm. From the zeta-potential measurements, the sonication increases the stability of the GF dispersion [27]. The negative value is attributed of the alkali content of GF (see Section 3.3). The discrepancy between the PSR (Table 5) and PSD (Fig. 4) resulted from residual agglomeration of the GF and SF when the APS measurements were taken.

3.3. Chemical composition

Table 6 presents the chemical compositions of the main oxides in the GF and SF. Compared to the SF, the GF had a lower silica (SiO_2) content and significant contents of lime (CaO) and alkalis ($Na_2O + K_2O$).

The loss on ignition (LOI) was determined for the GF and SF with TGA-MS. The GF and SF have a LOI of 3.7% and 1.8% respectively. Fig. 5 exhibits the TGA-MS plots of GF. The black curve is associated to with the weight loss as a function of temperature, well known as the TG curve. It uses the left-hand side vertical axis. The grey curve

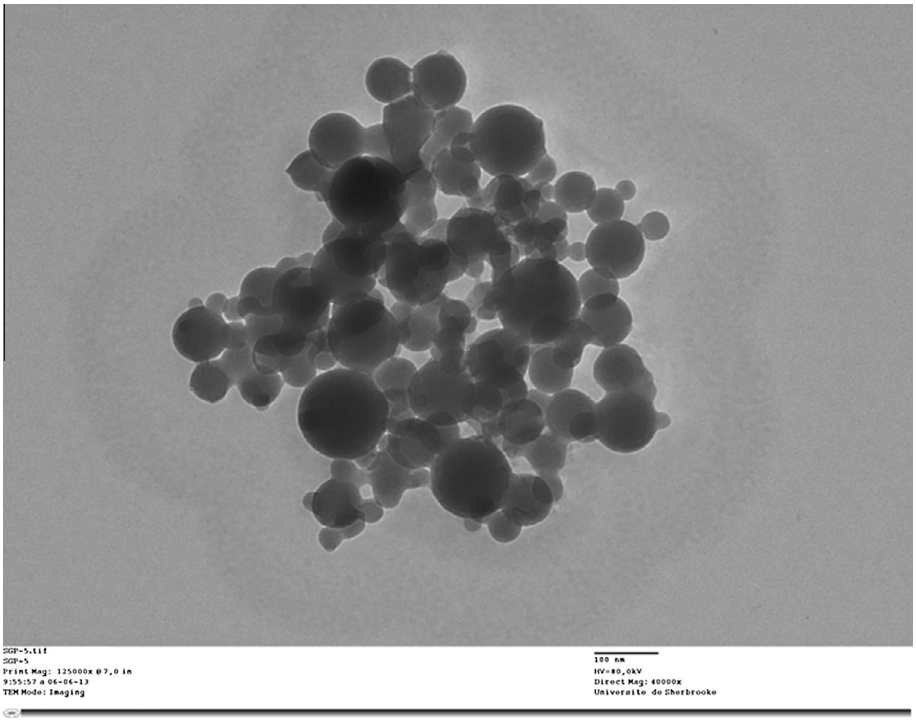

Fig. 2. TEM micrograph of GF nanoparticles using 40,000× magnification.

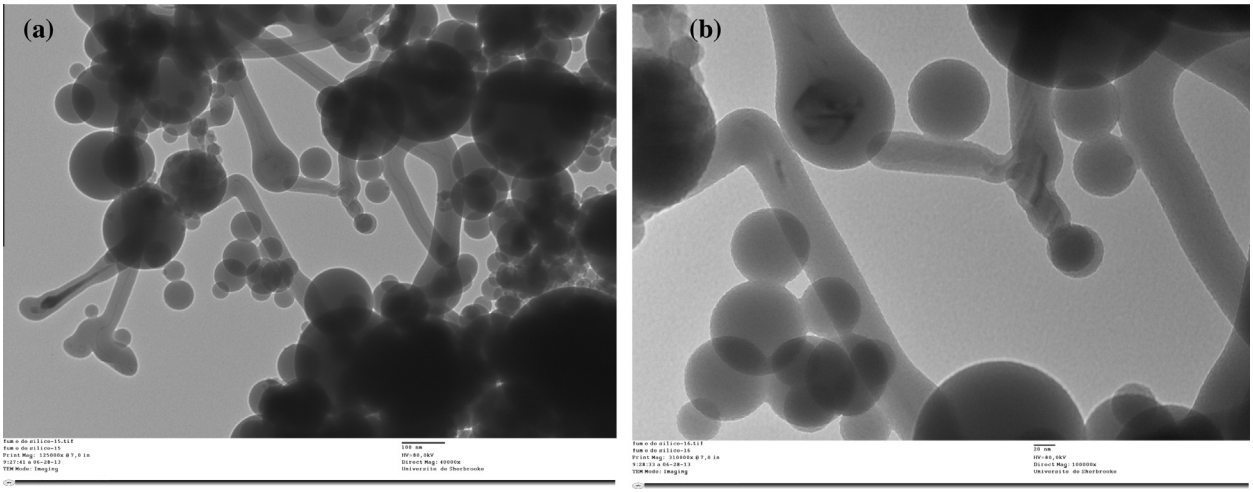

Fig. 3. TEM micrograph of SF nanoparticles using (a) 40,000× and (b) 100,000× magnifications.

Table 5
SSA, PSR, and nanocontent of GF and SF.

	SSA (m^2/kg)	PSR		Nano wt.%*
		Nano (nm)	Micro (μm)	
GF	16,500	30–200	1–10	97%–98%
SF	21,600	30–200	0.5–0.6	97%

* The balance is the microparticle content.

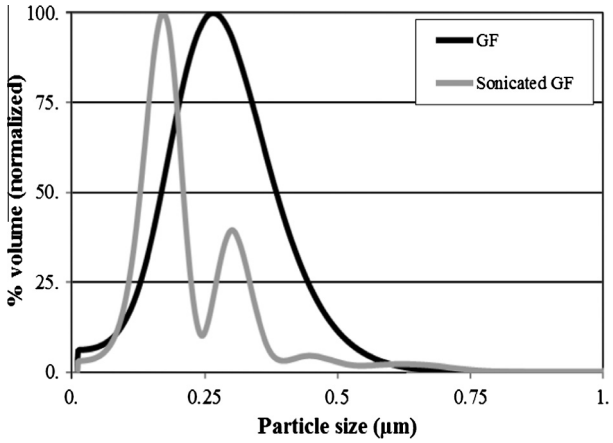

Fig. 4. Particle-size distribution of the nanometric fraction of the GF and GF dispersed by sonication.

is the MS measurement of mass 18 (H_2O) of the TGA exhausted gas and uses the right-hand vertical axis. The plot clearly shows the weight loss is mainly associated to a dehydration process. The MS signal increases with the weight-loss. The first mass occurring between 35 °C and 130 °C, corresponds to the removal of physically absorbed water. Further mass loss that started from the end of first mass loss till about 390 °C might be attributed to the removal of chemically absorbed water. The third mass drop from 390 °C till around 615 °C might be related to the dehydration of silanol group [31].

3.4. Crystallinity

In addition to high fineness and silica content, SCMs must generally have an amorphous microstructure in order to yield high reactivity in a cementitious matrix. As well known in the case SF (Fig. 6b), GF keeps its amorphous microstructure from waste glass (Fig. 6a). The XRD diffractograms in Fig. 6 show a hump between $2\theta = 15°$ and $2\theta = 40°$ centered on the location of the main peak of cristobalite (one form of crystallized SiO_2 stable at high temperature) and no distinguishable crystalline line from the background noise from $2\theta = 40°$ to $2\theta = 70°$.

Table 6
Chemical oxide composition of the GF and SF measured with XRF.

Metal oxide	GF	SF
SiO_2	70.65	96.51
Na_2O	11.72	0.07
CaO	10.59	0.65
Al_2O_3	1.58	0.20
MgO	0.68	0.25
K_2O	0.52	0.42
Fe_2O_3	0.26	0.06
TiO_2	0.05	0.00
Mn_3O_4	0.02	0.01

4. Tests on the cement pastes

4.1. Semiquantitative XRD method

Fig. 7 presents a typical result for the full XRD diffractogram of the $X13_{GF}$ mix. The XRD patterns of the $X13_{GF}$ pastes tested after 1, 7, and 28 days of hydration have been overlaid on this figure. The dry-powder mixes were also tested for calibration purposes. While the Calibration XRD diffractogram (before hydration) shows peaks solely for CH and the halo due to the amorphous GF, the patterns for 1, 7, and 28 days of hydration also reveal peaks for calcite ($CaCO_3$) and semicrystalline C–S–H. From these four diffractograms, the most intense CH peak at $2\theta = 34.09°$ was selected to calculate the CH peak intensity and CH consumption by the SCMs. Fig. 7 indicates that the CH peak intensity decreased as function of hydration age, confirming the reactivity of the GF with CH. The same procedure was applied to the other 43 XRD diffractograms obtained with the other mixes.

Fig. 8 presents a graph of the major CH peak (at $2\theta = 34.09°$) intensity versus the initial CH concentration for the different hydration durations for GF + CH and SF + CH mixes. The calibration curves for both the GF + CH and SF + CH mixes indicate that the intensity of the CH peak is proportional to the initial CH concentration. Using the linear fit of these two curves, the residual CH con-

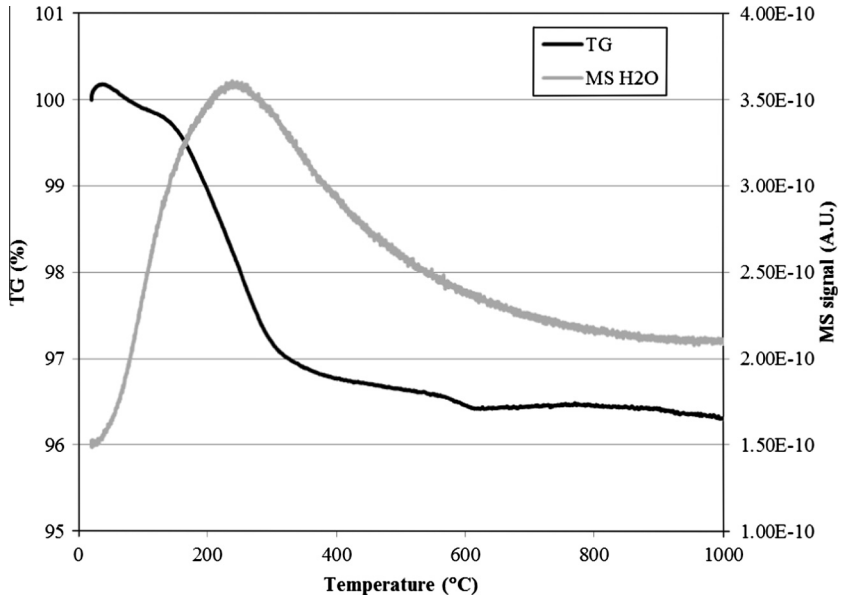

Fig. 5. TGA-MS analysis of GF. TG curve (black) is associated to the left-hand side vertical axis, the MS H_2O signal curve (grey), to the right-hand side vertical axis.

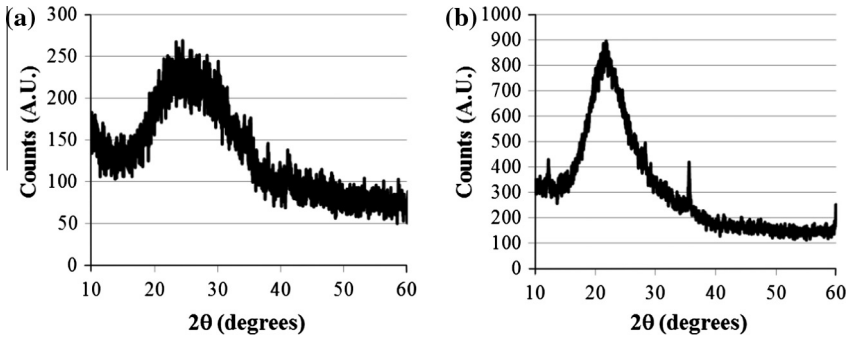

Fig. 6. XRD diffractogram of the (a) GF and (b) SF.

tent in each mixture can be computed as a function of the hydration time and initial CH content:

$$\text{SF}: \quad CH_{SF} = \frac{I_i}{73.08}$$

$$\text{GF}: \quad CH_{GF} = \frac{I_i}{65.08}$$

where CH_{SF} and CH_{GF} are the residual CH contents in the SF + CH and GF + CH mixes, and I_i, the intensity of the CH peak at a given *i* hydration time in days. For each curve, the residual CH in wt.% is indicated by the vertical axis on the right-hand side of Fig. 8.

After 1 day of hydration, the CH peak intensities for the GF + CH mixes were smaller than that of the SF + CH mixes, revealing a higher CH consumption by the GF at early age. CH consumption had completed for the $X5_{GF}$ and $X5_{SF}$ mixes. The $X23_{GF}$ mix had a CH content of ≈6.2 wt.%, while the $X23_{SF}$ mix had a CH content of ≈10.2 wt.%. At 7 days, the GF's consumption of CH appears to have slowed down compared to the values at 28 days, while CH consumption had been completed in all the SF mixes. The CH was also completely consumed in the SF + CH mixes at 28 days. The curve for SF + CH 28 days curve was thus omitted to alleviate Fig. 8. The GF had completed CH in the mixes with an initial CH content of <15 wt.%. The mixes with higher initial CH contents—$X17_{GF}$, $X20_{GF}$, and $X23_{GF}$—indicated residual CH contents of ≈0.5, 1.1, and 1.8 wt.%, respectively.

This limitation of GF in fixing CH seems to be related to its chemical composition. This can be verified by computing a chemical balance using the chemical content in SiO_2 and CaO for SF and GF in Table 6. For the case with higher initial content in CH, mix $X23_{SF}$ fixed 0.24 mol of Ca per mol of Si (Ca/Si = 0.24).

By taking into account the initial content in CaO for GF and the residual CH content at 28 days, mixes $X13_{GF}$, $X17_{GF}$, $X20_{GF}$, and $X23_{GF}$ have a Ca/Si molar ratio of 0.33, 0.42, 0.43 and 0.47 respectively. From these results, SF and GF look unsaturated in calcium for Ca/Si below than at least 0.33 and can continue to fix CH. At a value between 0.42 and 0.47, GF starts to be saturated in calcium. Although the Ca/Si slightly increases with the initial CH content, the GF ability in fixing CH is slowed down.

Fig. 9 shows VPSEM micrographs at different magnifications (1000× and 2500×) of the $X13_{GF}$ mixes after 28 days. The micrographs reveal the presence of GF particles and C–S–H gel, located around the GF microparticles where it formed. This also confirms the complete consumption of CH. The micrographs do not show any CH crystals.

4.2. Thermal analyses

The hardened cement-paste samples listed in Table 2 were tested with TGA/DTA for combined water and portlandite content. As an example, Fig. 10 presents the TGA/DTA/DTG plots of the $T10_{GF}$ paste after 56 days of curing. The plot shows three curves

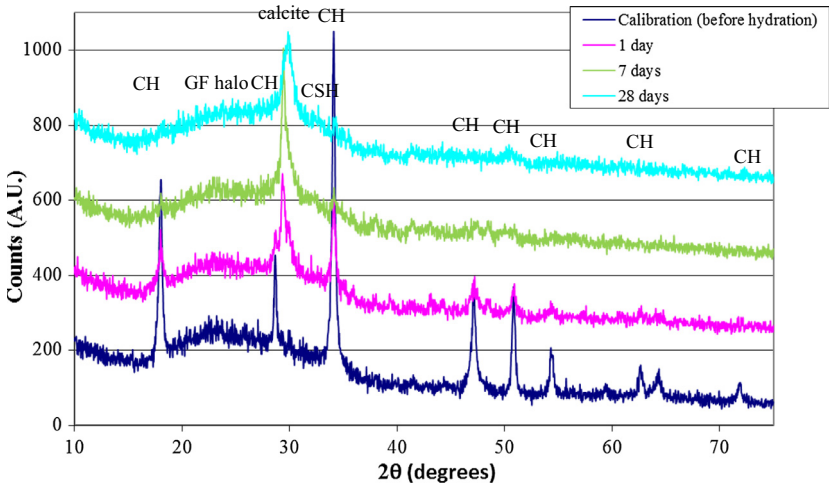

Fig. 7. XRD diffractogram for the $X13_{GF}$ mix as function of hydration age.

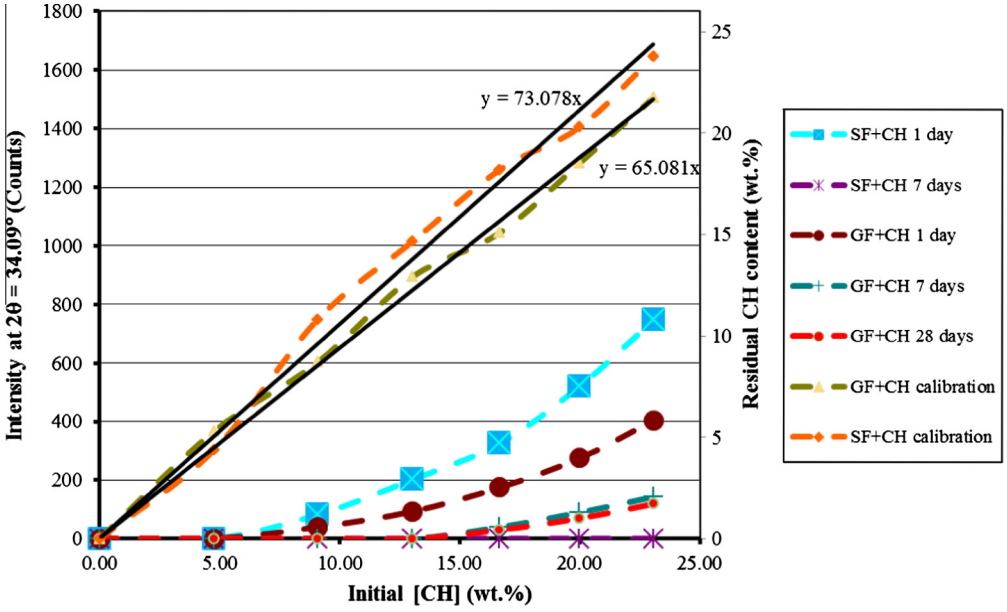

Fig. 8. CH peak intensity at $2\theta = 34.09°$ (left y-axis) and residual CH content (right y-axis) as function of initial CH concentration and hydration age.

as a function of temperature. The black curve is the TG curve. It uses the left-hand-side vertical axis. The grey curve represents the DTA curve and uses the first right-hand-side vertical axis. The dashed black curve plots the DTG and uses the second right-hand-side vertical axis. Weight losses from 50 °C to 150 °C, 150 °C to 400 °C, 400 °C to 450 °C, and 450 °C to 1000 °C are associated with the free water content, combined water content, CH dehydration, and carbonated content, respectively. From the DTG curve, the TGA micro-balance experienced some instability in the 850–950 °C range. Fig. 11 presents the evolution of the CH content as a function of curing time.

The CH content is calculated with the following equation:

$$\text{CH content}(\text{wt.}\%) = w \times \frac{\text{MW}_{\text{CH}}}{\text{MW}_{\text{H}_2\text{O}}}$$

where w is the weight loss between 400 °C and 450 °C, MW_{CH} and $\text{MW}_{\text{H}_2\text{O}}$, the molecular weights of CH and H_2O.

At early age (<7 days), the pastes containing the GF revealed a rapid increase in CH contents (Fig. 11). The pastes containing the GF point to a drastic reduction in CH content after 7 days (Fig. 11). This reduction in CH can be attributed to the pozzolanic reaction being triggered. From day 15 to day 56, the CH content gradually increased as the cement hydrated. At 56 days, $T5_{GF}$ and $T10_{GF}$ indicated similar CH contents, while T0 had a 70% higher CH content.

4.3. Isothermal calorimetry

Fig. 12 shows the evolution of the heat of hydration for the first 24 h for C0, $C10_{SF}$, and $C10_{GF}$ at W/B = 0.4. In these tests, the initial peak is attributed to the cement dissolution peak ($t < 1$ h). We did not take this peak into account in analyzing the results because the pastes were mixed outside the calorimetry cells. The second peak (5–6 h) is associated with the hydration of C_3S. The shoulders evident after 7 h are attributed to the hydration of C_3A and the forma-

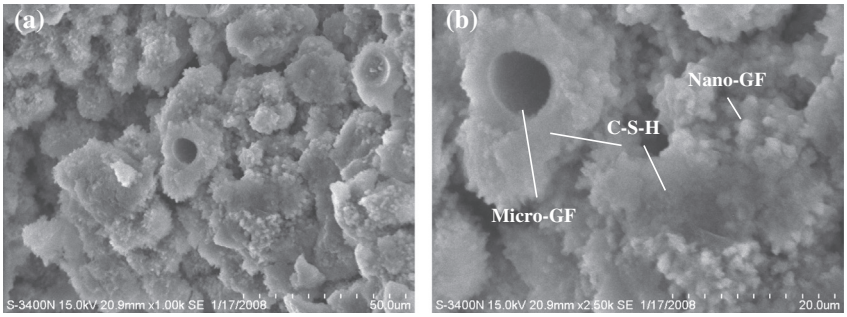

Fig. 9. Microstructure of $X13_{GF}$ after 28 days of hydration (a) at low magnification (1000×) and (b) at high magnification (2500×).

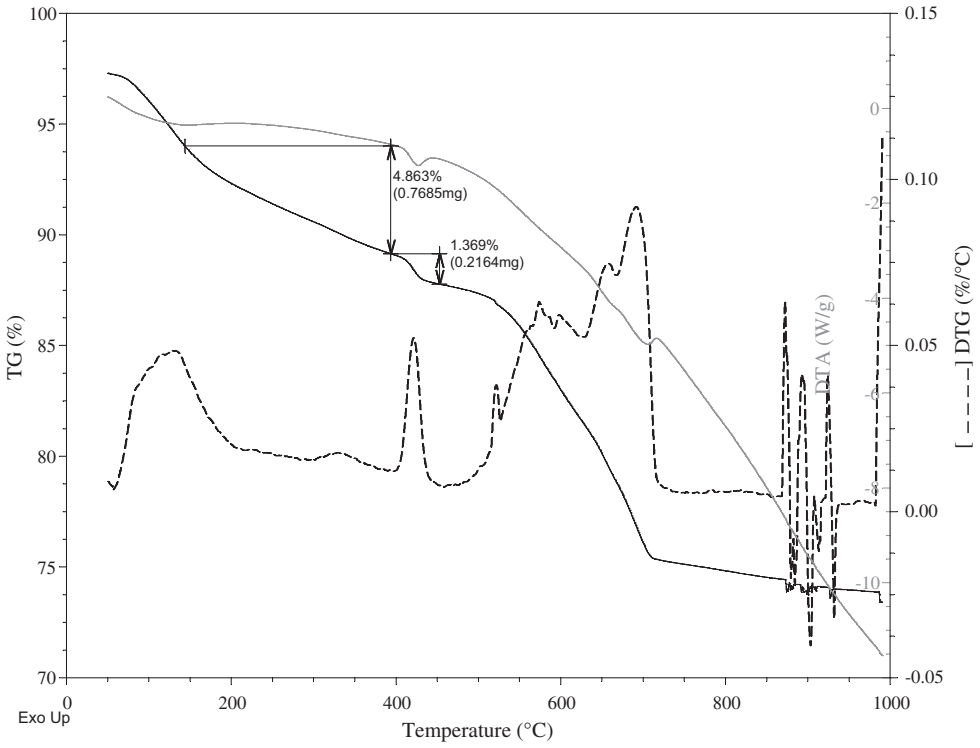

Fig. 10. TG/DTA/DTG plot of theT10GF 10% cement paste after 56 days of curing. TG curve (black) is associated to the left-hand side vertical axis, the DTA curve (grey), to the first right-hand side vertical axis, and the DTG curve (dashed black), to the second right-hand side vertical axis.

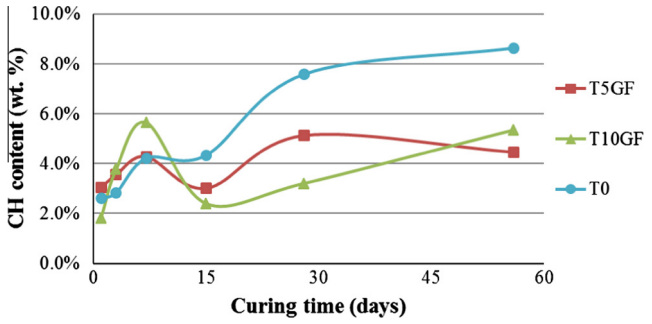

Fig. 11. Evolution of the CH content of the cement pastes as a function of curing time.

tion of ettringite (AFt) and calcium monosulfoaluminate crystals (AFm) [26].

Fig. 13 shows the evolution of the heat of hydration for the first 24 h for $C1_{GF}$ and $C5_{GF}$, and resembles the curves for the C0 and the $C10_{GF}$ pastes at W/B = 0.4.

In Fig. 12, the addition of the GF and SF accelerated the hydration of C_3S, giving the most exothermic curves at early age. The $C10_{GF}$ and $C10_{SF}$ pastes achieved a maximum heat of ≈4 mW/g at 6.3 h and 6.7 h, respectively, whereas the C0 paste had a maximum heat of 3.7 mW/g at 7.4 h. From 10 to 12 h until the end of the test, the $C10_{GF}$ paste was the least exothermic.

Fig. 13 shows that the $C1_{GF}$ curve is comparable to that of the C0 control curve, with $C5_{GF}$ having a slight increase in evolved heat at both the second and third peaks. Its shoulder, also remarked in Fig. 12 is especially 18% higher in evolved heat, occurring 2 h before in $C1_{GF}$ and C0. The $C10_{GF}$ is clearly the most exothermic and its second peaks appeared ≈1.5 h earlier than in either $C1_{GF}$ or C0. Its evolved heat per g of binder at the second and third peaks is approximately 10% higher than that of $C1_{GF}$ and C0. As noted by Gaitero et al. [14] and Thomas et al. [32], an increase of evolved heat and acceleration of C_3S hydration have also been noted with higher nanoparticle contents.

Fig. 14 presents the total heat of hydration after 24 h for all the pastes tested. The results indicate that increasing the GF content increased the total heat of hydration. When the cement-

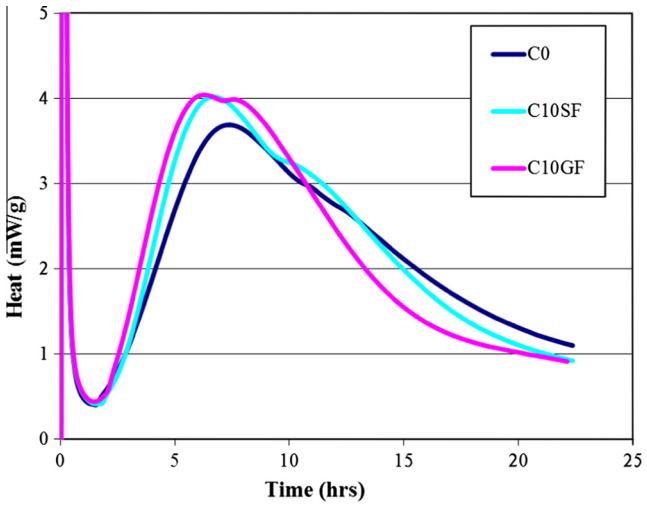

Fig. 12. Heat of hydration over time for C0, $C10_{SF}$, and $C10_{GF}$ at W/B = 0.4.

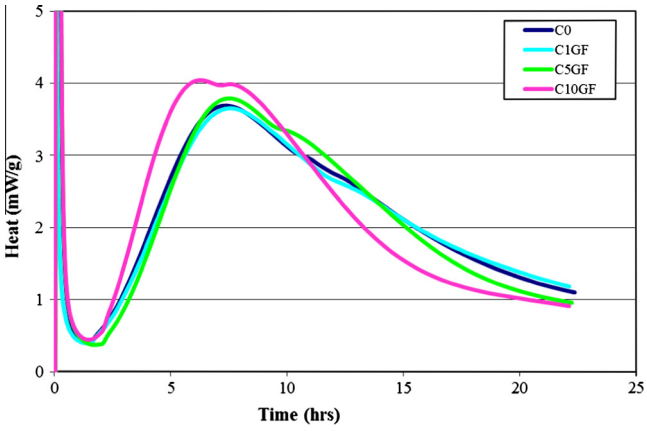

Fig. 13. Heat of hydration for C0, $C10_{SF}$, and $C10_{GF}$ at W/B = 0.4.

replacement level was lower than 5%, the total heat of hydration was lower than that of C0. With a 5% cement replacement, the total heat of hydration is similar to that of C0. With a 10% cement replacement, the total heat of hydration was 2% higher than that of C0 and 3% lower than that of $C10_{SF}$.

5. Tests on mortars

5.1. W/B = 0.484

As shown in Table 4 at W/B = 0.484, the use of the SF and GF increased the SP demand with respect to the control mortar $M0_A$. The $M10SF_A$ mortar was dosed with 1.6 times more SP than $M0_A$ to achieve a slump 30% lower (%flow). The $M10GF_A$ was dosed with 1.4 times more SP to achieve a slump 20% lower than $M0_A$.

Fig. 15 presents compressive strength of mortar cubes at 7, 28, 91 and 180 days. On the whole time range, Mortars $M1GF_A$ and $M5GF_A$ evidenced compressive strengths similar to $M0_A$ over the entire time range, while $M10GF_A$ and $M10SF_A$ exhibited higher compressive strengths at early (7 days) and later ages ($\geqslant$28 days). The average compressive strengths of $M10GF_A$ were respectively 13%, 52%, 46%, and 48% higher at 7, 28, 91 and 180 days than those of $M0_A$. In the case of $M10SF_A$, the average compressive strengths were respectively 42%, 50%, 69%, and 49% higher than those of $M0_A$ at 7, 28, 91, and 180 days, respectively. It should be noted that

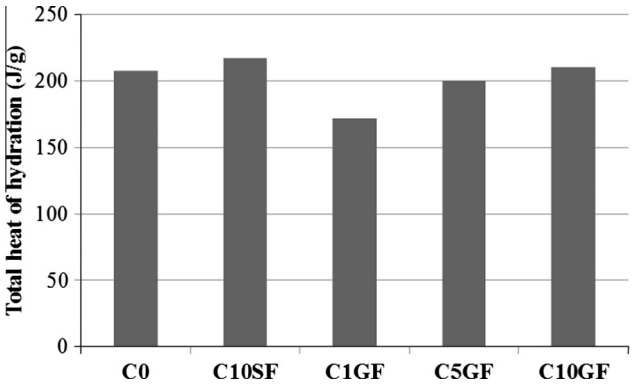

Fig. 14. Total heat of hydration of the tested cement paste for the first 24 h.

the compressive strength of $M10SF_A$ reached a plateau after 91 days. At 7 days, the higher compressive strength for $M10GF_A$ correlates with the high CH content calculated in Section 4.2 and the high heat of hydration determined in Section 4.3. At 28 days, the compressive strength of $M10GF_A$ was comparable to that of $M10SF_A$, while lower at 91 days and gradually reaching similar compressive strength after 180 days.

5.2. W/B = 0.4

Due to a better densification of the cementitious matrix at lower W/B, the compressive strengths are overall higher in Fig. 16 and were followed from 7 to 91 days. Even with a small percentage of GF (up to 5%), the compressive strength increased compared to $M0_B$. At early age, GF is again active. After 7 days, the compressive strengths of $M1GF_B$ and $M5GF_B$ were similar to that of $M5SF_B$. At 28 days, the compressive strengths of $M1GF_B$ and $M5GF_B$ were, respectively, 14% and 8% lower than that of $M5SF_B$. At 91 days, $M1GF_B$ and $M5GF_B$ achieved compressive strengths comparable to that of $M5SF_B$. At this age, the compressive strengths of $M1GF_B$ and $M5GF_B$ were, respectively, 14% and 19% higher than that of $M0_B$. A GF cement replacement of 10% ($M10GF_B$) decreased the compressive strength of mortars in comparison to $M5GF_B$.

5.3. Electrical conductivity (σ_E) of the pore solution

Fig. 17 presents the electrical-conductivity (σ_E) measurements for the pore solution in $M0_B$, $M5SF_B$, $M1GF_B$, and $M5GF_B$ during the first 24 h after the initial contact between the water and binder. The figure shows four distinct hydration phases. The first corresponds to an increase of σ_E during the first 4–6 h. This phase ends at the circles in Fig. 17. This phase is related to the dissolution of the various species in the pore solution, and the first peak and the induction period in Figs. 12 and 13. The second phase occurs in the circle labels, where the σ_E values kink. This corresponds to the precipitation of the first crystals of CH once the pore solution had reached an oversaturation level in Ca^{2+} ions. This kink in σ_E has been associated with the end of the induction period and the beginning of the mortar setting. The third phase starts past the circle labels and ends at the inflection point located in the square label. In this third phase, σ_E drops rapidly and quasi-linearly. This phase corresponds to the structuration of the hydrated cement paste in the mortar. This phase has also been associated with the second peak in Figs. 12 and 13. At the inflection point, σ_E reaches a minimum; the first compressive-strength testing of the mortar can be performed [26]. In the fourth phase, a small σ_E hump (except in M0) is framed by the inserted square. This hump relates to the decomposition of AFt, the formation of Afm, and the release

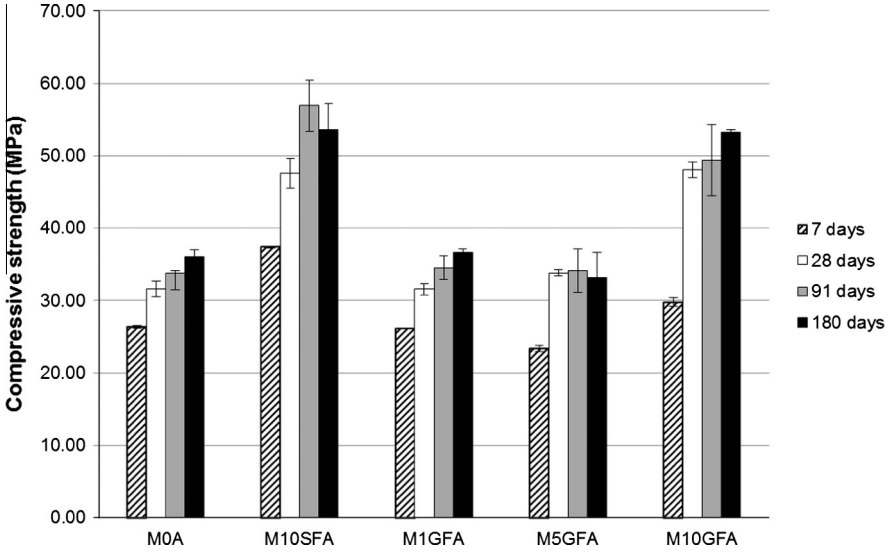

Fig. 15. Compressive strength of the mortars at W/B = 0.484.

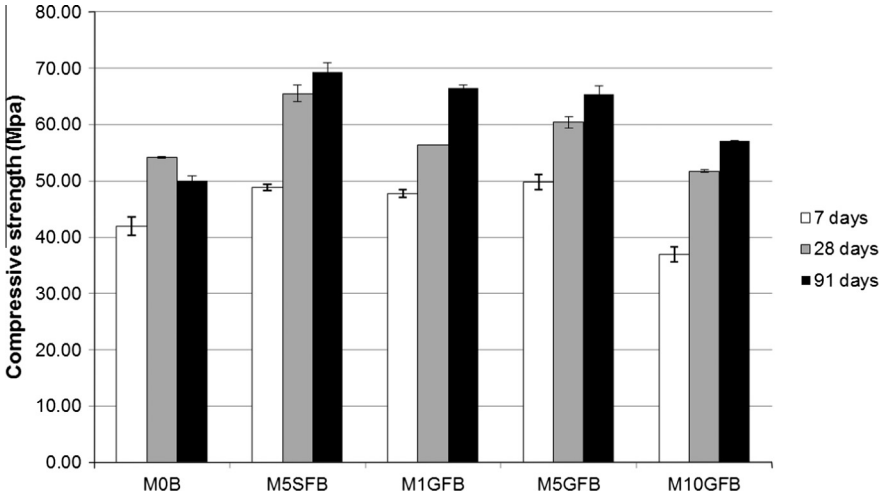

Fig. 16. Compressive strength of mortars at W/B = 0.40.

of alkalis trapped in the C_3A network [26]. It has been associated with the third peak in Figs. 12 and 13.

During the first phase, the σ_E in $M0_B$ increased more rapidly and ended sooner (after ≈3.6 h). $M5SF_B$ showed the weakest increase in σ_E. Indeed, σ_E and first-phase duration both increased when the GF content in the mortar increased. The σ_E of $M5GF_B$ even reached a value approaching that of $M0_B$ at the end of the first phase (after ≈5.5 h). The kink in the second phase occurs at 3.6, 4.6, 4.4, and 5.5 h in M0, $M5SF_B$, $M1GF_B$, and $M5GF_B$, respectively. The third phase lasted between 8.2 and 8.8 h for all the mortars. The humps in the fourth phase appear at 19.0, 19.6, and 18.2 h for $M5SF_B$, $M1GF_B$, and $M5GF_B$, respectively. M0 did not have such hump.

5.4. Mortar microstructure

Fig. 18 presents low magnification VP-SEM micrographs of mortars at W/B = 0.484 after 180 days of curing. The use of fine amorphous silica particles (SF and GF) in Figs. 18b and c, densified both the cement paste and the interfacial transition zone (ITZ) at the interface between the paste and sand particles. Overall, the ITZ was thinner and the cement paste appeared denser in $M10SF_A$ and $M10GF_B$ than in $M0_A$. In the case of $M0_A$ (Fig. 18a), the cement paste contained many small pores and a thicker ITZ with CH crystals.

Fig. 19 shows high magnification VP-SEM micrographs of the same site of interest exhibited in Fig. 18. In Fig. 19a, the $M0_A$ presents a poorer densification of the cement paste and of the ITZ than observed in $M10SF_A$ (Fig. 19b) and $M10GF_A$ (Fig. 19c). The cement paste contains many pores of 5–20 μm and ITZ of 3–10 μm thick. In Fig. 19b and c, the paste is well densified and the ITZ is thinner. Moreover, the ITZ look partially filled with SF and GF in these cases. The size of the ITZ for $M10SF_A$ and $M10GF_A$ is between 3 μm and 5 μm and between 1 μm and 7 μm respectively.

Fig. 20a shows a few micrometric GF particles hydrating within the cement paste. Observations did not evidence GF flocculation in the mortar. One of these particles has been enlarged to a magnification of 3.5 k times in Fig. 20b. The GF particles hydrated at a slower rate than the nanometric GF and SF, since they are distinguishable in the paste. In Fig. 20b, a rim of gel can be seen around the GF particle.

Fig. 21 presents the EDS spectra measured on points 1 (center of GF particle), 2 (gel rim), and 3 (cement paste) in Fig. 20b. From points 1 to 3, the sodium peak decreased and the calcium peak increased with respect to the silicon peak. The EDS spectrum at

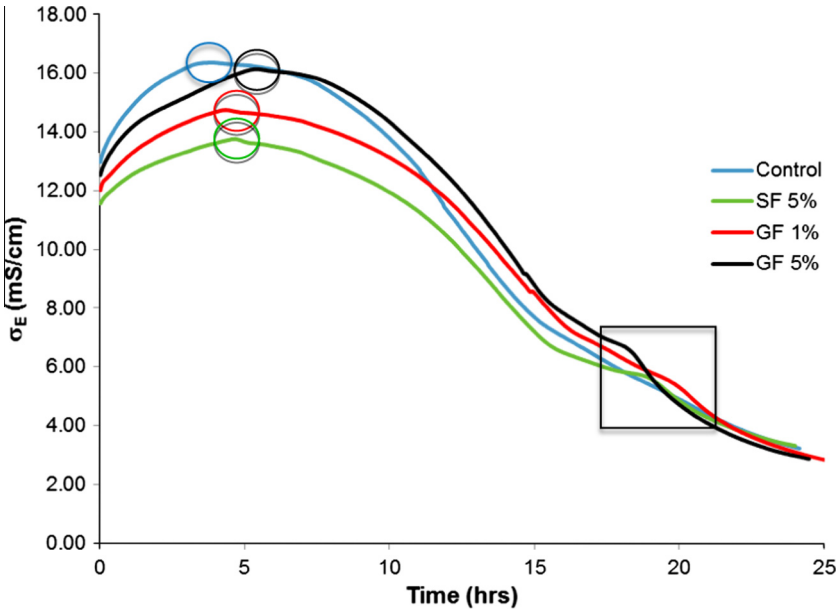

Fig. 17. σ_E as a function of hydration time.

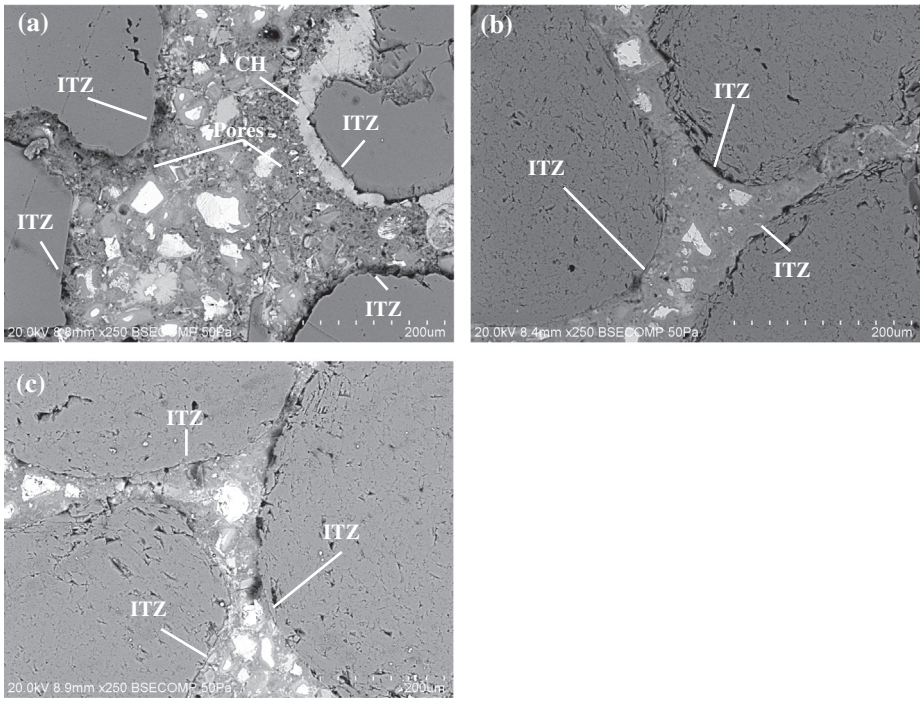

Fig. 18. VPSEM micrographs at low magnification for (a) $M0_A$, (b) $M10FS_A$ and (c) $M10GF_A$ after 180 days of curing.

point 2 indicates that the gel rim had a slightly richer calcium content and a slightly poorer sodium content than measured on point 1. The calcium oxide over silica ratios (C/S) are 0.22, 0.48 and 2.16 on points 1, 2, 3 respectively. The gel rim on point 2 consisted of pozzolanic C–S–H, while that on point 3, hydraulic C–S–H with CH.

Fig. 22 shows the EDS line scan plots for silicon (Fig. 21a) and calcium (Fig. 21b) scanned on the line formed from point 1 to 3 (EDS scan line), as indicated in Fig 20b. These line scan plots represent the EDS peak intensity as a function of the location on the EDS scan line. This line is 13 μm long. Point 1 is located at 0 μm and point 3 at 13 μm. The gradual increase in intensity of the silicon and the gradual decrease in calcium can be seen as the line scan enters in the GF particle (point 1).

6. Discussion

Sections 3–5 presented the characterization of the GF in pastes and mortars. In the cement pastes, the GF was mixed with CH (GF + CH mixes) as a cement replacement to study the pozzolanic reaction with TGA/DTA and isothermal calorimetry tests to study both the hydration and pozzolanic reactions. In these mortars, the compressive strength and σ_E were measured as a function of the GF

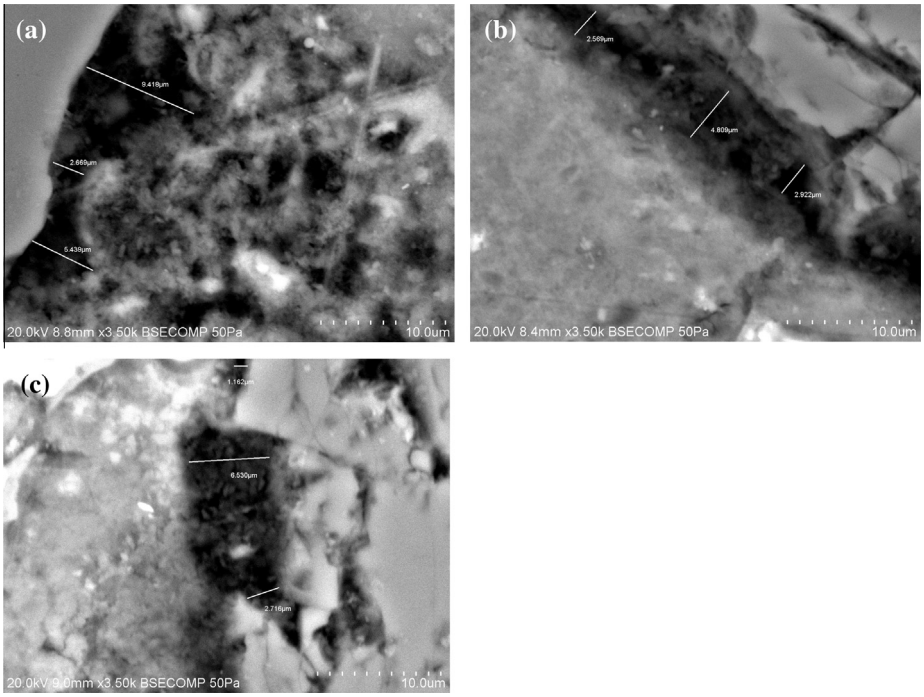

Fig. 19. VPSEM micrographs at high magnification for (a) $M0_A$, (b) $M10FS_A$, and (c) $M10GF_A$ after 180 days of curing.

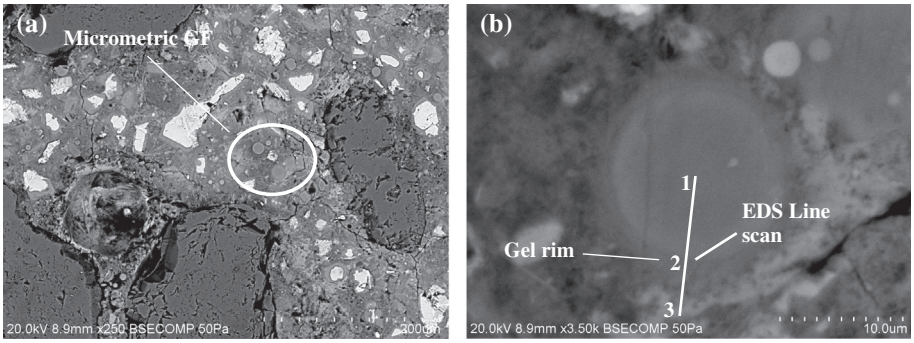

Fig. 20. VPSEM micrographs of $M10GF_A$ at low (a) and high magnification (b) after 180 days of curing with a focus on GF particles.

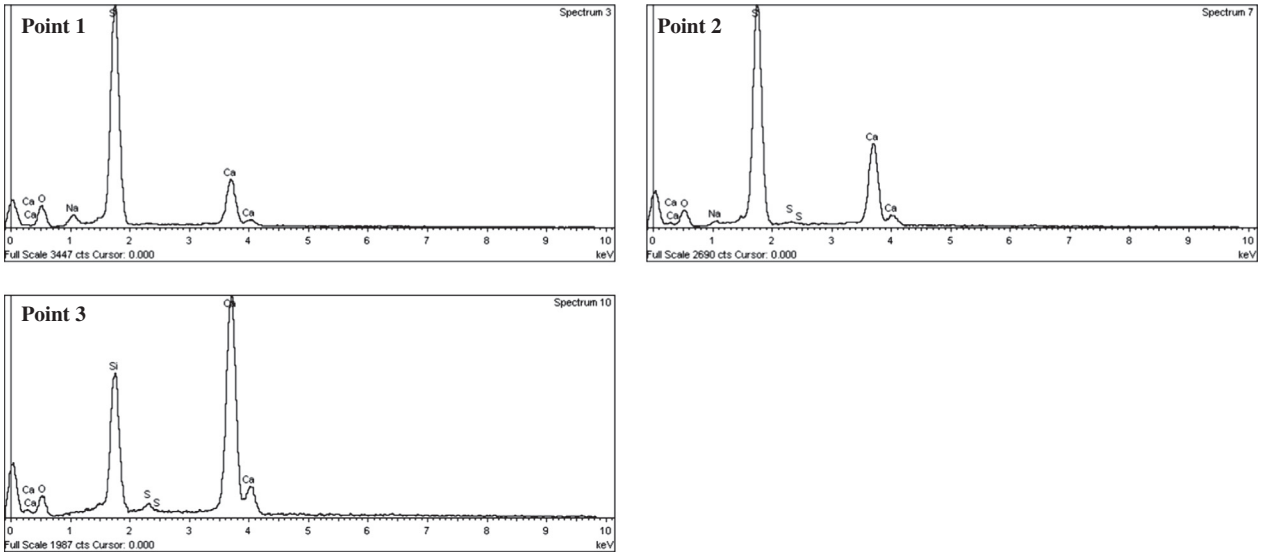

Fig. 21. EDS spectra measured at points 1, 2, and 3 in Fig. 20b.

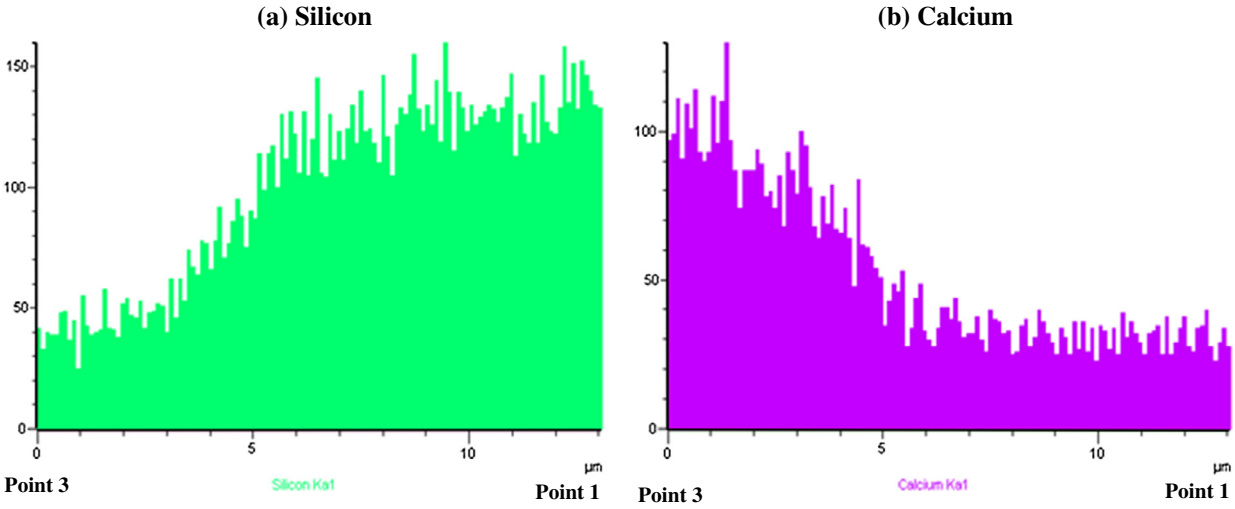

Fig. 22. EDS line scan between points 1 and 3 in Fig. 20b: (a) silicon and (b) calcium.

content as a cement replacement. VPSEM was used to observe mortar microstructure. In both the paste and mortar tests, the GF evidenced similar active behavior with short (<7 days) and long (>15 days) curing times. Indeed, on the short term, GF activates cement hydration, and, on the long term, it triggers a pozzolanic reaction.

6.1. Short-term phenomena

The non-negligible high alkali content in GF—more or less 12 wt.% (Table 6)—must be taken into account. Moreover, GF releases a high amount of its alkali content into the pore solution. Once in solution, GF can release up to 40% of its alkali content [33]. The increase of σ_E (Fig. 17) has thus been related to a higher concentration of alkalis in the pore solution provided by the GF. The $M5GF_B$ mortar took almost 2 more hours to reach M0's σ_E value, meaning that alkalis were released at slower rate than the dissolution of the cement-ion species in the pore solution.

Alkalis in the pore solution are known to activate cement hydration and the dissolution of aluminate phases [34]. Based on our isothermal-calorimetry measurements, the increased GF content in cement pastes hastened the appearance of the third peak in comparison to C0 and $C10_{SF}$ (Figs. 12 and 13), in which the SF had a negligible alkali content (Table 6). This observation is often made in the literature when amorphous nanosilica-based fume and nanoparticles are used in cementitious materials [34] and correlates with the σ_E measurements. As for the σ_E measurements, the hump in phase 4 (Fig. 17) also appeared earlier when the GF content increased and in comparison to $M5SF_B$. An increase in alkali normally leads to an increase in OH^- ions to balance the pore solution. The production of OH^- ions is often associated with an early precipitation of AFt, which is then converted into Afm [34]. Such precipitation removes sulfates from the pore solution. Because of its large SSA (Table 5), GF can also absorb sulfate ions [35]. Therefore, due to the lack of sulfates in the pore solution, C_3A is directly converted into Afm earlier, as shown by isothermal calorimetry (Figs. 12 and 13) and σ_E measurements (Fig. 17).

The large SSA of GF (Table 5) also contributes in activating the hydration reaction. Once the alkalis have been dissolved, GF offers nucleation sites for CH. When cement is put in contact with water, dissolved Ca^{2+} ions preferentially nucleate on the amorphous silica nanoparticles before precipitating in the pore solution. This favors the dissolution of anhydrous species from the cement [12,14,26,32], allowing cement hydration to proceed. Cement-based materials, however, need a certain threshold content of GF, depending on the W/B, in order to achieve the nucleation effect. For instance, a dosage of 1% and 5% in the GF in the cement pastes did not lead to a clear improvement in the heat of hydration, while a dosage of 10% did (Figs. 13 and 14). In the case of $C1_{GF}$ and $C5_{GF}$, the low dosage in GF does not provide enough alkalis and nucleation sites for the cement hydration and its dissolution effect is dominant. In the case of $C10_{GF}$, the C_3S peak occurred more rapidly with a greater exothermic value (Figs. 12 and 13). With $M5GF_B$, the delay of the kink in the σ_E curve in phase 1 was more pronounced than for M0 and $M1GF_B$, as well as $M5SF_B$ (Fig. 17). This can be explained by a higher amount of CH formed when cement hydration progressed, as evidenced by the TGA/DTA tests (Fig. 11). As seen previously [22,36–37], the mechanical strength of cement-based materials increased rapidly on the short term (Figs. 15 and 16).

6.2. Long-term phenomena

While the short term activity of GF is attributed to its alkali activation of the cement hydration and its available nucleation sites for CH, thermal analyses and tests on mortars suggested that the, the pozzolanic reaction is triggered during the 14–28 days time frame. A drastic reduction in CH can be observed in the GF cement pastes in comparison to the T0 control (Fig. 11). Although $T5_{GF}$ and $T10_{GF}$ indicate similar CH contents, a higher dissolution of cement by the GF activated the pozzolanic reaction and the cement hydration reaction could proceed.

The semiquantitative XRD results (Fig. 8) and compressive strengths of the mortars (Fig. 15 and 16) show that the GF had slower reactivity than the SF, but helped achieve compressive strengths comparable to those obtained in the SF mortars at the last tested ages. The GF has a lower SSA (Table 5) and contains 17–18% less silica (Table 6) than the SF. This weight by percentage is partially compensated by alkalis. Having less amorphous silica available reduces the kinetics of the pozzolanic reaction. The compressive strengths of the mortars also improved after a threshold content of GF had been reached. Based on the calorimetry measurements (Fig. 13), $C1_{GF}$ and $C5_{GF}$ did not clearly improve the heat of hydration in comparison to C0. Similarly, dosages of 1% and 5% GF in mortars at a W/B = 0.484 ($M1GF_A$, $M5GF_A$) yielded equivalent compressive strengths to that of the control (M0). With a dosage of 10%, $M10GF_A$ clearly showed improved compressive strengths, similar to those of $M10SF_A$ (Fig. 15). The GF's high alkali content

did not affect the ultimate compressive strength of the mortars, as has been seen with plain cement concrete [34]. Like SF [38–40], GF entraps alkalis in C–S–H gels. VPSEM observations show that the GF and SF densified the mortar's microstructure and reduced the ITZ (Figs. 18a,b and 19a, b). They react with CH to produce pozzolanic C–S–H gels that plugged the pores in the cement paste.

Overall, the GF mortars required a lower SP dosage than the SF mortars. This fact can be attributed to the GF's completely spherical morphology (Fig. 1 and 2). This morphology enabled a ball-bearing effect in the fresh-mortar batches. In the case of the SF, the non-negligible nanofilament content (Fig. 3) greatly reduced this effect. At low W/B, a high GF content in the mortar (e.g., $M10GF_B$) decreased the compressive strength in comparison to mortars with lower GF contents (e.g., $M1GF_B$, $M5GF_B$). The SP dosage in $M10GF_B$ exceeded the manufacturer's prescribed limit, which retarded the setting of this mortar and reduced the degree of hydration of its cement content (Table 4 and Fig. 16). It should be noted that most cement and concrete producers in Canada [41,42] limit the use of materials such as SF to 8%.

6.3. Reaction mechanisms

Thomas et al. [32] stated that silica-based materials have a two-stage reaction mechanism. First, they react with calcium ions dissolved from cement to form C–S–H gels. Second, the latter turn into seeds for the hydration process of cement. In our case, the GF exhibited a four-stage mechanism when mixed with cementitious materials. First, the alkali contents activated the dissolution of the cement phases and their hydration (Phase 1 in Fig. 17). Second, the GF acted as a nucleating agent for CH at early age (Phase 2 in Fig. 17). Third, the GF triggered the pozzolanic reaction (Fig. 11). Fourth, the alkalis were fixed in the C–S–H gels by the GF (Figs. 15 and 16). The effects of GF on the properties of cement-based materials are therefore determined by the amount of alkalis dissolved in the pore solution and by the SSA available for the nucleation effect and the pozzolanic reaction to take place. The properties of cement-based materials are therefore not improved below a certain threshold of GF content determined by the W/B and mortar compacity [43,44].

7. Conclusion

The use of GF in cement-based materials was investigated as a valuable, viable alternative to SF. The actual scarcity and high cost of SF reduces the opportunity for its use in high- and ultra-high-performance concrete. The GF reported herein was produced using the RF ICP spheroidization process for waste glass. Because of its high throughput, this technology can provide a commercially viable alternative to existing SF and exert low environmental impact when produced with renewable electricity sources. The GF tested presented PSDs similar to the SF, although their morphologies differ. The GF had a completely spherical morphology, whereas the SF exhibited a non-negligible content of nanofilaments. It contained amorphous spheroidized glass nanoparticles with a PSD of 30–200 nm. The GF, however, contained a non-negligible amount of alkalis.

On the short term, these alkalis dissolved in the pore solution during the first hours of hydration. They activated the dissolution and hydration of the calcium silicates and calcium aluminate phases of the cement. Because of its large SSA, the GF played the role of a nucleating agent. At early age, the hydration of C_3S and C_3A phases was more exothermic and the GF consumed ≈4% more CH than the SF. Above a threshold level of GF content in cement pastes, the saturation in CH in the pore solution is delayed and the hydration of C_3S and C_3A hastened. These activation effects favor cement hydration.

On the long term (>28 days), the amorphous silica of the GF reacted slowly with CH via the pozzolanic reaction. A drastic decrease in CH was measured in the GF cement pastes. Above a threshold level of GF content in the mortars, an adequate amount of GF reacted with CH to yield pozzolanic C–S–H, thereby yielding compressive strengths comparable to those obtained with the SF mortars.

The tests performed on the cement pastes and mortars indicate that the GF had a four-stage behavior when mixed with cement-based materials. First, the alkali content activated the dissolution of the cement phases and their hydration. Second, the GF acted as a nucleating agent for CH at early age. Third, the GF triggered the pozzolanic reaction at late age. Fourth, the GF entrapped the alkalis in the C–S–H gels. The properties of GF cement-based materials are driven by the amount of alkalis dissolved in the pore solution and quantity of SSA for the nucleation effect and pozzolanic reaction. In order to yield improved effects, the GF content must be above a threshold level determined by the W/B and the material compacity in cement-based materials.

Acknowledgements

We are grateful to the Société des Alcools du Québec (SAQ) Industrial Research Chair on the Valorization of Waste Glass in Materials for its financial support.

References

[1] N. Adam, P.C. Aïtcin, PC, high performance concrete. An overview, Mater. Struct. 31 (206) (1998) 111–117.
[2] P. Richard, M. Cheyrezy, Composition of reactive powder concretes, Cem. Concr. Res. 25 (7) (1995) 1501–1511.
[3] A. Tagnit-Hamou, S. Soliman, A.F. Omran, M.T. Mousa, N. Gauvreau, F. Provencher, Novel ultra-high-performance glass concrete, Concr. Int. 37 (3) (2015) 41–47.
[4] A. Behnood, H. Ziari, Effects of silica fume addition and water to cement ratio on the properties of high-strength concrete after exposure to high temperatures, Cem. Concr. Compos. 30 (2) (2008) 106–112.
[5] R. Siddique, Utilization of silica fume in concrete: review of hardened properties, Resour. Conserv. Recycl. 55 (2011) 923–932.
[6] O.E. Gjorv, P.J.M. Monteiro, P.K. Mehta, Effect of condensed silica fume on the steel-concrete bond, ACI Mater. J. 87 (1990) 573–580.
[7] P.C. Aïtcin, P. Laplante, Long-term compressive strength of silica-fume concrete, J. Mater. Civ. Eng. 2 (1990) 164–170.
[8] M. Mazloom, A.A. Ramezanianpour, J.J. Brooks, Effect of silica fume on mechanical properties of high-strength concrete, Cem. Concr. Compos. 26 (2004) 347–357.
[9] C.S. Poon, S.C. Kou, L. Lam, Compressive strength, chloride diffusivity and pore structure of high performance metakaolin and silica fume concrete, Constr. Build. Mater. 20 (2006) 858–865.
[10] A. Cwirzen, V. Penttala, Aggregate–cement paste transition zone properties affecting the salt–frost damage of high-performance concretes, Cem. Concr. Res. 35 (4) (2005) 671–679.
[11] J.A. Rossignolo, Interfacial interactions in concretes with silica fume and SBR latex, Constr. Build. Mater. 23 (2) (2008) 817–821.
[12] F. Sanchez, K. Sobolev, Nanotechnology in concrete – a review, Constr. Build. Mater. 24 (2010) 2060–2071.
[13] A. Porro, J.S. Dolado, J.J. Gaitero, H. Manzano, Nanotechnology and concrete: concepts and approach, Transp. Res. Rec., 2142 Nanotechnol. Cem. Concr. 2 (2010) 127–129.
[14] J.J. Gaitero, I. Campillo, P. Mondal, P. Shah, Small change can make a great difference, Transp. Res. Rec. 2141 (Nanotechnol. Cem. Concr.) 1 (2010) 1–5.
[15] M. Amin, K. Abu el-hassan, Effect of using different types of nano materials on mechanical properties of high strength concrete, Constr. Build. Mater. 80 (2015) 116–124.
[16] H. Du, S. Du, X. Liu, Durability performances of concrete with nano-silica, Constr. Build. Mater. 73 (2014) 705–712.
[17] E. García-Taengua, M. Sonebi, K.M.A. Hossain, M. Lachemi, J. Khatib, Effects of the addition of nanosilica on the rheology, hydration and development of the compressive strength of cement mortars, Compos. B 81 (2015) 120–129.
[18] M. Sonebi, E. García-Taengua, K.M.A. Hossain, J. Khatib, M. Lachemi, Effect of nanosilica addition on the fresh properties and shrinkage of mortars with fly ash and superplasticizer, Constr. Build. Mater. 84 (2015) 269–276.

[19] F. Kontoleontos, P.E. Tsakiridis, A. Marinos, V. Kaloidas, M. Katsioti, Influence of colloidal nanosilica on ultrafine cement hydration: physicochemical and microstructural characterization, Constr. Build. Mater. 35 (2012) 347–360.
[20] H. Madani, A. Bagheri, T. Parhizkar, The pozzolanic reactivity of monodispersed nanosilica hydrosols and their influence on the hydration characteristics of Portland cement, Cem. Concr. Res. 42 (2012) 1563–1570.
[21] M.-H. Zhang, J. Islam, Use of nano-silica to reduce setting time and increase early strength of concretes with high volumes of fly ash or slag, Constr. Build. Mater. 29 (2012) 573–580.
[22] J.S. Dolado, I. Campillo, E. Erkizia, J.A. Ibanez, A. Porro, A. Guerrero, S. Goñi, Effect of nanosilica additions on belite cement pastes held in sulfate solutions, J. Am. Ceram. Soc. 90 (12) (2007) 3973–3976.
[23] A.S. Brykov, R.T. Kamaliev, M.V. Mokeev, Influence of ultradispersed silicas on portland cement hydration, Russ. J. Appl. Chem. 83 (2) (2010) 208–213.
[24] D. Harbec, F. Gitzhofer, A. Tagnit-Hamou, Induction plasma synthesis of nanometric spheroidized glass powder for use in cementitious materials, Powder Technol. 214 (2011) 356–364.
[25] R. Pristavita, R.J. Munz, T. Addona, Transferred arc production of fumed silica: rheological properties, Ind. Eng. Chem. Res. 47 (2008) (2008) 6790–6795.
[26] P.-C. Aïtcin, Binders for Durable and Sustainable Concrete, Taylor & Francis, 2008. Modern Concrete Technology Series.
[27] E.D. Rodriguez, L. Soriano, J. Paya, M.V. Borrachero, J.M. Monzo, Increase of the reactivity of densified silica fume by sonication treatment, Ultrason. Sonochem. 19 (2012) 1099–1107.
[28] A. Alhozaimy, G. Fares, A. Al-Negheimish, M.S. Jaafar, The autoclaved concrete industry: an easy-to-follow method for optimization and testing, Constr. Build. Mater. 49 (2013) 184–193.
[29] O. Bonneau, C. Vernet, M. Moranville, P.-C. Aïtcin, Characterization of the granular packing and percolation threshold of reactive powder concrete, Cem. Concr. Res. 30 (2000) 1861–1867.
[30] J. Zhang, S. Seeger, Silica/silicone nanofilament hybrid coatings with almost perfect superhydrophobicity, ChemPhysChem 14 (8) (2013) 1646–1651.
[31] L.M. Mukundan, R. Nirmal, D. Vaikkath, P.D. Nair, A new synthesis route to high surface area sol gel bioactive glass through alcohol washing: a preliminary study, Biomatter 3 (2) (2013) 24288.
[32] J.J. Thomas, H.M. Jennings, J.J. Chen, Influence of nucleation seeding on the hydration mechanisms of tricalcium silicate and cement, J. Phys. Chem. C 113 (2009) 4327–4334.
[33] A. Pavoine, D. Harbec, M. Tohoue Tognonvi, A. Tagnit-Hamou, The co-alkali activation of class F fly ash with nano- and micro- waste glass powder, Cem. Concr. Compos., submitted CCC-D-15-00093.
[34] I. Jawed, J. Skalny, Alkali in cement: a review II. Effects of Alkalies on Hydration and Performance of Portland Cement, Cem. Concr. Res. 8 (1978) 37–52.
[35] G. Land, D. Stephan, The influence of nano-silica on the hydration of Portland cement, J. Mater. Sci. (2011), http://dx.doi.org/10.1007/s10853-011-5881-1.
[36] L. Raki, J. Beaudoin, R. Alizadeh, J. Makar, T. Sato, Cement and concrete nanoscience and nanotechnology, Materials 3 (2010) 918–942.
[37] G. Li, Properties of high-volume fly ash concrete incorporating nano-SiO_2, Cem. Concr. Res. 34 (2004) 1043–1049.
[38] J. Dushesne, M.-A. Bérubé, The effectiveness of supplementary cementing materials in suppressing expansion due to ASR: another look at the reaction mechanisms Part 2: Pore solution chemistry, Cem. Concr. Res. 24 (1994) 221–230.
[39] M.H. Shehata, M.D.A. Thomas, Use of ternary blends containing silica fume and fly ash to suppress expansion due to alkali-silica reaction in concrete, Cem. Concr. Res. 32 (2002) 341–349.
[40] M. Thomas, The effect of supplementary cementing materials on alkali-silica reaction: a review, Cem. Concr. Res. 41 (2011) 1224–1231.
[41] Ciment Québec, Ciment hydraulic compose binaire type GUb-8SF, Certificat d'Analyse, April 2014.
[42] Lafarge Cement, Ciment Type GUb-8SF, Rapport Client, September 2012.
[43] F. de Larrard, T. Sedran, Optimization of ultra-high-performance concrete by the use of a packing model, Cem. Concr. Res. 24 (6) (1994) 997–1009.
[44] F. de Larrad, T. Sedran, Mixture-proportioning of high-performance concrete, Cem. Concr. Res. 32 (11) (2002) 1699–1704.